The Astrophysical Journal, 859:169 (7pp), 2018 June 1 https://doi.org/10.3847/1538-4357/aac109

Periodic Recurrence Patterns In X-Ray Solar Flare Appearances

N. Gyenge[1,2,3] and R. Erdélyi[1,3]
[1] Solar Physics and Space Plasmas Research Centre (SP2RC), School of Mathematics and Statistics, University of Sheffield Hounsfield Road, Hicks Building, Sheffield S3 7RH, UK; n.g.gyenge@sheffield.ac.uk
[2] Debrecen Heliophysical Observatory (DHO), Research Centre for Astronomy and Earth Sciences, Hungarian Academy of Sciences, Debrecen, P.O. Box 30, H-4010, Hungary
[3] Dept. of Astronomy, Eötvös Lórand University, Pázmány Péter sétány 1/A, Budapest, H-1117, Hungary
Received 2018 February 26; revised 2018 April 25; accepted 2018 April 25; published 2018 June 5

Abstract

The temporal recurrence of micro-flare events is studied for a time interval before and after of major solar flares. Our sample is based on the X-ray flare observations by the *Geostationary Operational Environmental Satellite* (*GOES*) and *Reuven Ramaty High Energy Solar Spectroscopic Imager* (*RHESSI*). The analyzed data contain 1330/301 M-class and X-class *GOES*/*RHESSI* energetic solar flares and 4062/4119 *GOES*/*RHESSI* micro-flares covering the period elapse since 2002. The temporal analysis of recurrence, by Fast Fourier Transform, of the micro-flares, shows multiple significant periods. Based on the *GOES* and *RHESSI* data, the temporal analysis also demonstrates that multiple periods manifest simultaneously in both statistical samples without any significant shift over time. In the *GOES* sample, the detected significant periods are: 11.33, 5.61, 3.75, 2.80, and 2.24 minutes. The *RHESSI* data show similar significant periods at 8.54, 5.28, 3.66, 2.88, and 2.19 minutes. The periods are interpreted as signatures of standing oscillations, with the longest period (P_1) being the fundamental and others being higher harmonic modes. The period ratio of the fundamental and higher harmonics (P_1/P_N) is also analyzed. The standing modes may be signatures of global oscillations of the entire solar atmosphere encompassing magnetized plasma from the photosphere to the corona in active regions.

Key words: Sun: activity – Sun: chromosphere – Sun: flares – Sun: oscillations – Sun: X-rays, gamma rays

1. Solar Atmospheric Oscillations

Achieving a detailed understanding of the nature of solar atmospheric intensity oscillations is a long-standing challenge. The intensity oscillations could provide vital information about the properties of the solar atmosphere (e.g., geometric structure, magnetic structure, density structure, ionization degree) by using solar magnetoseismology tools (Roberts et al. 1984; Banerjee et al. 2007; Erdélyi & Taroyan 2008; Andries et al. 2009; Verth et al. 2010; Jess et al. 2015). Numerous studies reported oscillations in the solar atmosphere, using high-resolution observations (De Moortel 2009; Ruderman & Erdélyi 2009; Banerjee et al. 2011; Wang 2011; Mathioudakis et al. 2013). The observed periods of intensity oscillations range from several minutes to several hours (Auchère et al. 2014). Various oscillation patterns with periods of a few dozens of minutes are also found in polar plumes and polar coronal holes observations (DeForest & Gurman 1998). Bocchialini et al. (2011) studied intensity and Doppler velocity oscillations and reported periods from several up to 80 minutes in filament and prominence observations. Tian et al. (2008) investigated solar bright points and reported oscillations between periods of 8–64 minutes. Magnetohydrodynamic (MHD) waves in the solar corona are often accounted for by the observed intensity oscillations in the range of 2–33 minutes (Aschwanden et al. 2002). Hence, long-period oscillations in the solar atmosphere are not unprecedented.

Smaller local features like solar flares are also able to produce periodic behavior, and studying their oscillatory patterns has become a well-studied subject (McLaughlin et al. 2018). In general, the observed periodic features in the wavelet power or the Fourier spectrum of the soft X-ray emissions are called quasi-periodic pulsations (QPPs). Based on the observations of the *Geostationary Operational Environmental Satellite* (*GOES*) satellite, Dolla et al. (2012) performed a case study that reported QPP signatures in the emission of an X-class solar flare. Simões et al. (2015) confirmed these results by analyzing a larger statistical sample. They demonstrated that 28 events out of 35 X-class flares also show QPP signatures. Reznikova & Shibasaki (2011) used *Reuven Ramaty High Energy Solar Spectroscopic Imager* (*RHESSI*) observations to show that periodicities in the range of 2.5–5.0 minutes become shorter the closer the observations are to a major energetic flare. Sych et al. (2009) found similar QPP periodicities and proposed that the source of the oscillations could be triggered by 3-minute slow magnetoacoustic waves. Sych et al. (2015) found continuous energy amplification of 3-minute waves in sunspot umbrae before a solar flare.

The observed oscillations in coronal loops may indicate that standing slow modes are likely triggered by micro-flares, which are produced by impulsive heating (Mendoza-Briceño et al. 2002; Taroyan et al. 2005; Erdélyi & Taroyan 2008). On the other hand, the micro-flares themselves before a major, energetic flare are usually called precursors (Charikov 2000) and their temporal distribution may be linked to other types of periodic variations of X-ray flux. Namely, the majority of the hard X-ray flares are preceded by precursors, usually a few dozens of minutes before the major solar flare (Tappin 1991). The information obtained by the observations of these flare precursors can be applied to acquiring the spatio-temporal properties of the local magnetic reorganization process and may also reveal diagnostic information about the nature of the destabilization of the active region.

In this work, we study the temporal distribution of solar flare (mostly micro-flare) recurrences before and after an energetic eruption. An energetic eruption, here, refers to X-type and

M-type solar flares. Micro-flare occurrence before or after a major flare will be referred to as pre-flare or post-flare activity. Furthermore, for the sake of simplicity, both types of micro-flares, pre-flares and post-flares, will be jointly referred to as minor flares.

2. Methodology

Two X-ray flare databases are employed in our study. First, the major flares and minor flares are provided by the *GOES* satellite. The *GOES* catalog contains information about the basic properties of the solar flares, such as the onset time, the position, the magnitude of the events, and the identification of the associated active region. The flare catalog is available at NGDC/NOAA.[4] Although the main focus is on the statistical population of *GOES* eruptions, a control sample is also used that is based on the flare list[5] by the *RHESSI* satellite (Lin et al. 2002). The *RHESSI* flare list contains data about the onset time of the flare, duration of the event, peak intensity, photon count, and energy channel of the maximal energy. The positions of the solar flares are calculated by 128×128 back-projection maps using 16 arcsec pixels (Hurford et al. 2003). The spatial resolutions may seem to be somewhat inaccurate, but the position data are sufficiently accurate for locating the active region. The *GOES* and *RHESSI* catalogs contain 25,691 and 121,430 solar flare events, respectively, for the analyzed time period between 2002 and 2017. The discrepancy between the number of observed solar flares may lie in the sensitivity of satellite detectors and/or the significance threshold of the signal-processing. Although, the identification definitions for solar flares are similar for both catalogs, the two satellites observe at slightly different wavelength ranges, which may also cause further discrepancies.

For identifying major flares for both the *GOES* and *RHESSI* samples, the following criteria are introduced. In the *GOES* statistical sample, only M- and X-class flares are selected as major flares. However, the *RHESSI* data do not contain flare classification. Therefore, the *RHESSI* major flare candidates must be associated with the *GOES* counterpart records for obtaining the flare classification information for each solar flare. Only simultaneously observed events are considered, i.e., the *RHESSI* and *GOES* solar flares must be relatively close in space and time. The actual information for *RHESSI* major flares is taken from the *RHESSI* flare database. The *GOES* flare counterpart event only assists in filtering the magnitude of the *RHESSI* observations. It is also required that no additional flare occurs with a larger peak flux in the same sunspot group within a 6 hr interval before and after the candidate major flare. A major flare candidate without an associated active region is not considered for selection for further analysis.

The final *GOES* sample obtained by applying the above criteria contains 1330 M-class and X-class events (including 1219 M-class and 111 X-class events) between 2002 and 2017. The final *RHESSI* statistical population consists of 301 major flares, 290 M-class and 11 X-class events between the same period as the *GOES* sample. Table 1 shows the number of major flare events before and after filtering. The total population of the *RHESSI* sample may seem somewhat low compared to the sample size of the *GOES* sample. Due to the orbital properties of the *RHESSI* satellite, half of the solar eruptions cannot be observed. A significant portion of the data are also lost because of the missing active region identification, the missing *GOES* counterpart flare association, the influence of the orbit of the *RHESSI* satellite, and other interferences, such as the South Atlantic Anomaly (Christe et al. 2008).

Table 1
Number of Major Events before and after Filtering

Source	Type	Before Filtering	After Filtering
GOES	M-class	1340	1219
GOES	X-class	115	111
Total		1455	1330
RHESSI	M-class	593	290
RHESSI	X-class	56	11
Total		649	301

Criteria for filtering the minor flares are also applied. The *RHESSI* satellite's orbit allows a 1-hour observation time then a 40-minute observation blackout caused by the satellite spending time in orbital eclipse. Furthermore, when the satellite passes through the intermediate southern latitudes, the detector counts are influenced by the South Atlantic Anomaly. Therefore, we omitted solar flares that occurred while crossing the South Atlantic Anomaly and data gaps. More specifically, the *RHESSI* eruptions indicated by the flags ED, EE, ES, DE, DS, DG, DE, GS, NS SD, SE, SS, and PS are omitted. Fortunately, the *GOES* flare catalog does not suffer periodic data gaps from the satellite orbit as do the *RHESSI* observations. When a minor flare occurs in the same sunspot group within at most 6 hr before or after the major flare, the eruption is automatically considered a minor flare of a major flare. However, the minor flares must be less energetic than the associated major flares. In the *GOES* sample, the flare classification of the minor flare candidate must be smaller than the classification of the major event. In the case of the *RHESSI* data, the highest energy band in which the minor event is observed must be smaller than the highest energy band of the major solar flare. At this stage, direct physical causality between the major and the minor flare cannot be assumed; however, both events could be a consequence of the reorganization of a local magnetic field. After applying our introduced filtering criteria, the total number of *GOES* minor flare events is 4062, containing 2290 pre-flares, and 1772 post-flares. Meanwhile, the *RHESSI* minor flare population is composed of 4119 events, including 1960 pre-flares and 2159 post-flares. Table 2 demonstrates the number of minor flare events before and after applying the filtering criteria.

Let us define the reference time as the moment of the major flare eruption for each active region. Next, the elapsed time between the eruption of a minor flare (t_i) and its major flare (t^*) is calculated for each major flare in every active region separately. Let us now introduce

$$A_n = \{(t_1 - t^*), (t_2 - t^*), (t_3 - t^*), \ ..., (t_i - t^*)\}, \qquad (1)$$

where A_n contains the time differences between the major and minor solar flares in each active region. The actual value of $(t_i - t^*)$ must be between -360 and 360 minutes, however, $0 \notin A$. The domain $[-360, 0[$ represents the pre-flares up to 6 hr prior to the major flare and] 0, 360] stands for the post-flares, up to 6 hr after the onset of the major event. The subscript n

[4] ftp://ftp.ngdc.noaa.gov/STP/space-weather/solar-data/solar-features/solar-flares/x-rays/goes/
[5] http://hesperia.gsfc.nasa.gov/hessidata/dbase/hessi_flare_list.txt

Table 2
Number of Minor Events before and after Filtering

Source	Type	M-class Major before Filtering	After Filtering
GOES	Pre-flare	2270	2102
GOES	Post-flare	1807	1675
Total		4077	3777
RHESSI	Pre-flare	4273	1851
RHESSI	Post-flare	4043	2067
Total		8316	3918
Source	Type	X-class Major before Filtering	After Filtering
GOES	Pre-flare	191	188
GOES	Post-flare	100	97
Total		291	285
RHESSI	Pre-flare	534	109
RHESSI	Post-flare	441	92
Total		975	201
Source	Type	All Major before Filtering	After Filtering
GOES	Pre-flare	2461	2290
GOES	Post-flare	1907	1772
Total		4368	4062
RHESSI	Pre-flare	4807	1960
RHESSI	Post-flare	4484	2159
Total		9291	4119

represents the number of major flares. The total number of elements for a given A_n equals the total number of pre-flares and post-flares. On average, each *GOES* major flare is surrounded by 3 *GOES* minor flares and each *RHESSI* major flare has 13 *RHESSI* minor flares. Hence, case studies based on a single active region cannot be performed. To increase the number of events we merge all major flares (n) in all active regions into set x. Therefore, the total statistical sample size is now defined by the expression

$$x = \bigcup_{i=1}^{n} A_i. \tag{2}$$

The frequency distribution $F(x)$ is calculated in one-minute bins of the 6 hr period before and after the main flare, therefore the number of bins is 720. In each bin, we determine the total number of minor flares. One bin still contains approximately half a dozen minor flares, more specifically in the *GOES* statistics each bin contains 5.6 solar flares on average. For the *RHESSI* population, 5.7 solar flares are present per bin on average. The frequency distribution $F(x)$ is normalized by the following definition (also referred to as Z-Scores):

$$Z(x_i) = \frac{F(x_i) - \overline{F(x)}}{\sigma(F(x))}, \tag{3}$$

where $\overline{F(x)}$ represents the mean of the frequency distribution $F(x)$ and $\sigma(F(x))$ is the standard deviation. The mean $\overline{F(x)} = 5.64$ and standard deviation $\sigma(F(x)) = 3.37$ for the *GOES* statistical population. The *RHESSI* sample shows the mean $\overline{F(x)} = 5.72$ and the standard deviation $\sigma(F(x)) = 3.20$. Finally, anomalies or outliers were identified and excluded from the further statistics, therefore we omitted peaks greater than the $|Z(x_i)| > 5\sigma$ threshold.

Panels (A) of Figures 1 and 2 show the time variation of the minor flare occurrence based on the *RHESSI* and *GOES* flares separately before and after the occurrence of the major event. Both time-series show an undesirable feature, namely the number of the minor flares is significantly decreased as the occurrence of the major flare is imminent. This behavior is likely to be the consequence of the enhanced particle emission by the major eruption. The particle emission of a major flare may surpass the fine dynamics of the reconnection in the same active region. The trend can be removed by applying the lag operator $LZ(x_t) = Z(x_{t-1})$. The first differences $\Delta Z(x_t)$ of the *RHESSI* and *GOES* populations are defined by

$$\Delta Z(x_t) = (1 - L)Z(x_t). \tag{4}$$

Panel (B) of Figure 1 shows the temporal variation of the *GOES* micro-flare Z-Scores after calculating the first difference of the time-series. The *GOES* signal is now suitable for frequency analysis. Unfortunately, the temporal variation of the *RHESSI* micro-flare occurrence histogram (panel (A) of Figure 2) also shows another unwanted feature. The period of this unwanted fluctuation is around 100 minutes. The period may be the consequence of the orbit of the *RHESSI* satellite, which features a 60-minute observational period followed by a 40-minute blackout.

The orbit itself therefore may influence our sampling method, hence the importance of the dominant 100-minute *RHESSI* oscillation cannot be certain. For that reason, the following additional analysis is performed. A virtual satellite is created *in silico*, which observes random eruptive events. The orbit of the virtual satellite features the same properties as the orbit of the *RHESSI* satellite, i.e., a 60-minute "observational" period and a 40-minute blackout. The occurrence and the magnitude of the major and minor flares are random, however, the total number of random events equals the number of real observed data. Hence, we modeled 301 major and 4119 minor eruptions. Let us now apply the same methodology used for previous analyses with this new random-based sample. Panel (A) of Figure 3 shows the result of the random-based sample statistics based on 10,000 simulations. Panel (B) of Figure 3 demonstrates the frequency domain signal, which (not surprisingly) reveals one dominant peak around 100 minutes (or around 0.17 mHz). Judging from only the *RHESSI* data set, it cannot be safely assumed that this period is only an artifact and there is no other physical process with a similar periodicity. The *GOES* statistical population, however, does not seem to show similar periodical behavior. Therefore, the 100-minute oscillation in the *RHESSI* data set can be confirmed as an artifact, which can be removed by applying the seasonal lag operator $L^S Z(x_t) = Z(x_{t-S})$. If the data show fluctuation patterns at every S observations, a seasonal difference can be applied to remove the seasonal trend from the time-series using the expression

$$\Delta^S Z(x_t) = (1 - L^S)Z(x_t). \tag{5}$$

Unfortunately, the seasonal lag operator introduces an unwanted consequence. The transformed signal is truncated and the range of signal is shorter than seen in the original. However, since the 100-minute orbital periodicity is so clear,

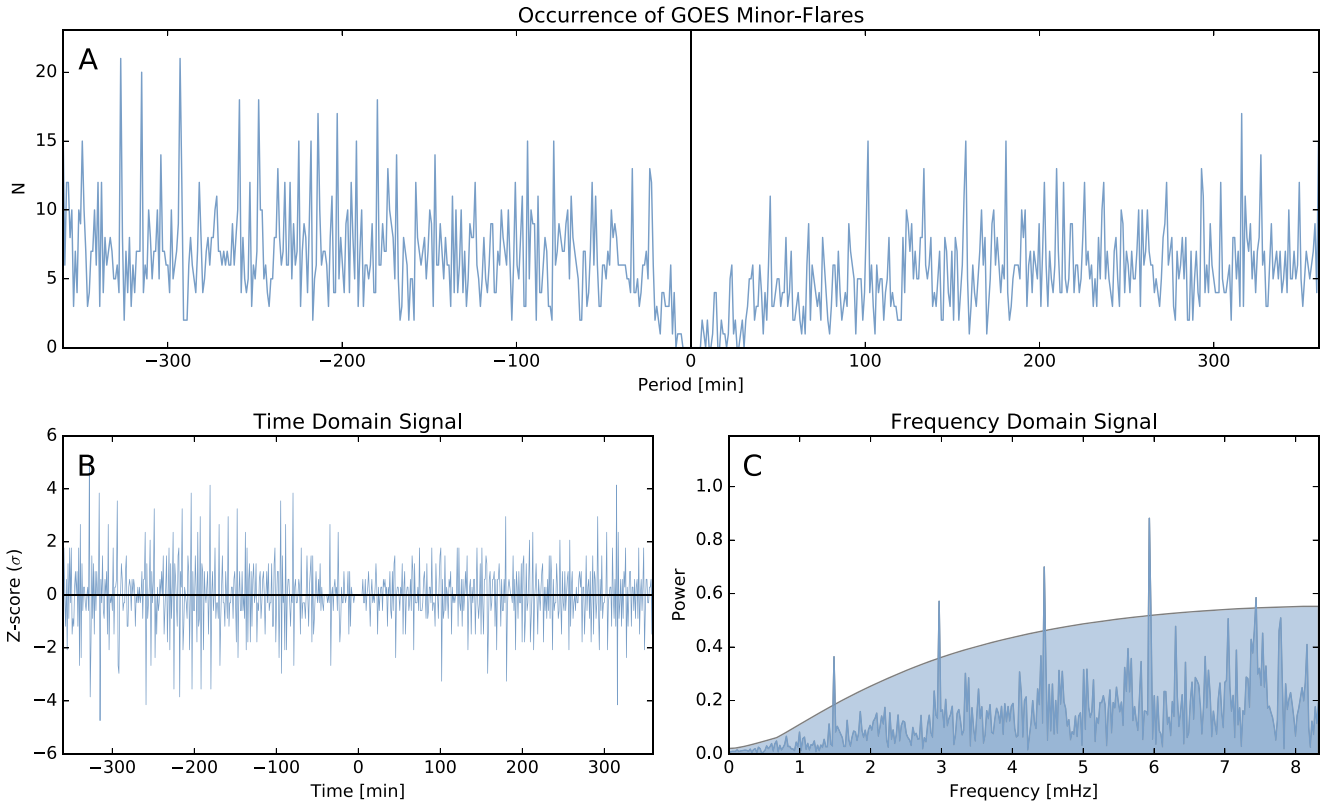

Figure 1. Panel (A) demonstrates the temporal variation of the pre-flare and post-flare occurrences before and after the major M-class or X-class flares based on the *GOES* flare data. Panel (B) represents the time domain signal. This signal is transformed by applying the first difference to the original signal. Panel (C) represents the power spectrum of the FFT. Under the blue area the peaks are not considered significant frequencies. These peaks are below the 3σ significant threshold.

the trend can be extrapolated forward in time before applying the operator, which preserves the time domain to ± 360 minutes. We have chosen a sine function as a model function for describing the orbital period of the *RHESSI* satellite. The seasonal lag operator is applied to the extended time-series. Therefore, the transformed signal remains in the range of ± 360 minutes and the orbital periodicity is removed as well. Panel (B) of Figure 2 shows the temporal properties of the *RHESSI* minor flare sample after applying the first differencing and seasonal differencing techniques. The transformed *RHESSI* and *GOES* time-series are now more suitable for frequency analysis because the results of the temporal analysis are less likely biased by artificial periods due to the applied sampling methods.

3. Frequency Analysis

We use fast Fourier transform (FFT) for studying the periodic behavior of the data. The stationarity time sample is required because the FFT algorithm is not able to reveal the local properties of the time–frequency space. By applying the first and seasonal difference methods, our time samples fulfill this requirement. Therefore, it is assumed that the periodic behavior of the signal is time-independent.

The significance level is calculated by employing an Autoregressive Model AR(1), also known as red noise or $1/f$ noise distribution (Weedon 2003). The red noise is a common assumption in astrophysical time-series. The power spectrum of the red noise is weighted toward the low frequencies, however, there is no preferred period over the range (Kasdin 1995). For estimating the significance of the peaks in the time–frequency space, we generated 1 million independent simulations based on the best-fit AR(1) models. We estimated the coefficients of the applied models. For the *GOES* statistics, the expression can be written as follows:

$$Z(x_t) = 0.2317 * Z(x_{t-1}) + \epsilon_t. \quad (6)$$

In case of *RHESSI* statistics, the fitted autoregressive AR(1) expression becomes

$$Z(x_t) = 0.2160 * Z(x_{t-1}) + \epsilon_t, \quad (7)$$

where the parameter $Z(x_t)$ is regressed from the previous value $Z(x_{t-1})$ and the parameter ϵ_t represents the error. The obtained expressions now can be used for generating simulations. Since the original data values are generally low numbers, the generated simulations are based on a Poisson distribution rather than being Gaussian. Finally, we applied the same methodology to real data, i.e., the simulated data are differenced and FFT is performed as well. The standard deviation and average in each frequency bin are calculated based on the 1 million simulations. In the further statistics, the significance level is defined by the total of the average and three standard deviations.

Panel (C) of Figure 1 shows the result of the period analysis based on the transformed *GOES*, which is presented by panel (B) of Figure 1. The power spectrum unveils multiple significant frequencies. The lowest frequency is now 1.47 mHz. The powers of the higher frequencies are more pronounced and the peaks appear at 2.97, 4.44, 5.94, and around 7.43 mHz. The sampling frequency is 16.65 mHz and the Nyquist frequency is 8.325 mHz. Therefore, the latest period is close to (but still below) the Nyquist frequency. Other frequencies close to the

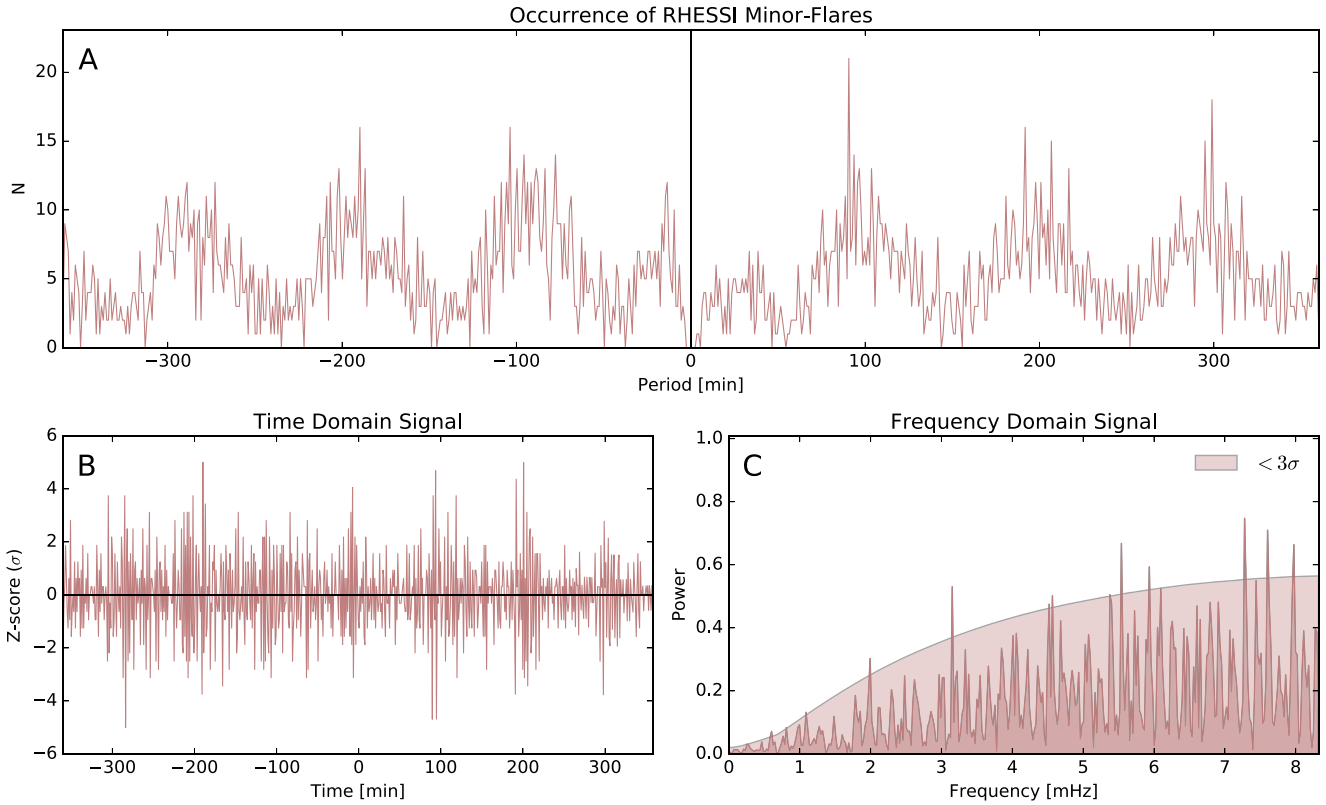

Figure 2. Panel (A) shows the time variation of the minor flare occurrences before and after the major flare based on the *RHESSI* statistical sample. Panel (B) demonstrates the transformed data by employing first difference and seasonal difference techniques. Panel (C) is the power spectrum of the FFT. Under the red area the peaks are not considered significant frequencies. These peaks are below the 3σ significance threshold.

significance level are also visible, such as 7.04 and 7.79 mHz. Their significance is still above the significance level 2σ, however, they are relatively close to another more significant peak. Therefore, these peaks are omitted from the statistics. Note that the signature of the noise in the power spectrum does not show red noise behavior. The error is weighted toward the high frequencies, which is a typical blue noise signature. The changed properties of the noise structure are more than likely to be the consequence of the data differentiation.

Panel (C) of Figure 2 displays the result of the frequency analysis based on the *RHESSI* flare population. Artificial periods (100 minutes or 45-minute fluctuations) due to the orbit of the *RHESSI* satellite and the influence of the South Atlantic Anomaly are removed from the original signal, hence significant peaks at 0.37 and 0.18 mHz are not detectable. Unfortunately, the previously detected 1.47 mHz *GOES* oscillation is also not detectable in these statistics. However, in the power spectrum of the *RHESSI* data, there is a significant oscillation around 1.95 mHz. The other *GOES* frequencies can be clearly verified by *RHESSI* observations. Clear and strong 3.15, 4.55, 5.78, and 7.2 mHz oscillations are found above the 3σ threshold. The 5.78 and 7.61 mHz oscillations are surrounded by several additional significant peaks; however, these peaks are relatively close to each other.

Table 3 and Figure 4 display a summary of the obtained peaks for both the *GOES* and *RHESSI* statistics. In Figure 4, the *GOES* statistics show five significant oscillation periods, labeled *G*0, *G*1, *G*2, *G*3, and *G*4. The *RHESSI* statistics displays five remarkable oscillations, labeled *R*0, *R*1, *R*2, *R*3, and *R*4. The periods *R*0, *R*1 and *R*2 are strong and remarkable oscillations with a single peak structure. However, the remaining two significant oscillations, *R*3 and *R*4, each contain three significant peaks. The differences between the first and last peaks in *R*3 and *R*4 are a few seconds, hence these peaks cannot be considered with a high confidence to be manifestations of different physical processes. These peaks are considered together and the oscillation period of the *R*3 and *R*4 clusters are calculated by the average of the peaks within. Table 3 shows the average periods of the obtained peaks.

The oscillations *G*1 and *G*2 are clearly confirmed by the peaks *R*1 and *R*2. The *G*1 and *R*1 periods show only a 6% difference and the difference between the *G*2 and *R*2 periods is only around 3%. The discrepancies for the average periods of the *G*3, *R*3 and *G*4, *R*4 peaks are also negligible (around 3% and 2%). However, the discrepancy between the longest period *R*0 and period *G*0 is around 24%.

4. Physical Interpretation

Let us now consider a simple oscillatory system: linear transversal waves in a one-dimensional uniform finite string with length L and fixed endpoints. When this system is perturbed, standing waves will form. The string has a number of specific frequencies, defined by the properties of the string, at which it will naturally vibrate. These frequencies are called eigenfrequencies, where the longest period is called the fundamental mode and the other modes are referred to as higher harmonics. For a uniform string, the fundamental mode

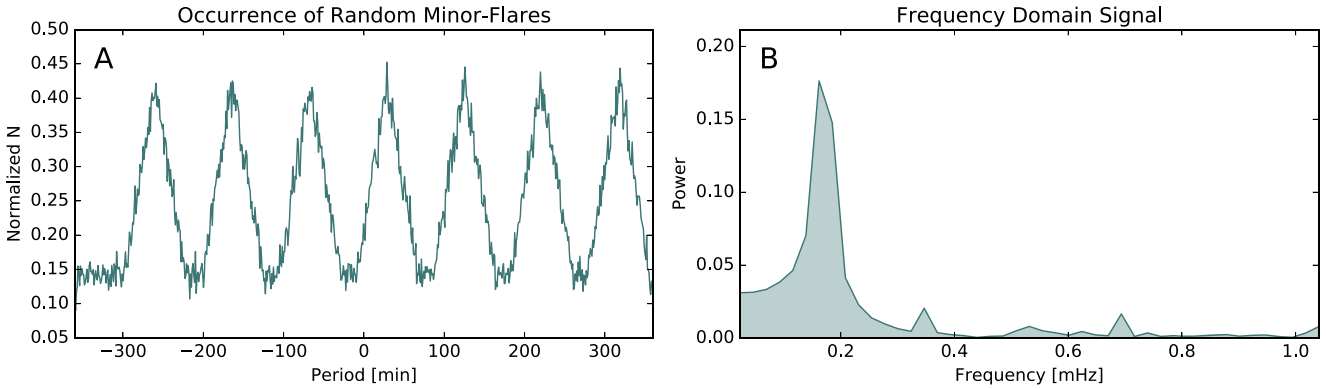

Figure 3. Random-based statistical population for demonstrating the effect of the *RHESSI* orbital period. The left panel shows the occurrence of the random population and the right panel demonstrates the frequency domain signal.

Table 3
Detected Oscillation Frequencies and Periods

N	Frequency [mHz]	Period [minutes]	ID.	Ratio P_1/P_N	Sample
1	1.47	11.33	G0	⋯	*GOES*
2	2.97	5.61	G1	2.01	*GOES*
3	4.44	3.75	G2	3.02	*GOES*
4	5.94	2.80	G3	4.04	*GOES*
5	7.43	2.24	G4	5.05	*GOES*
1	1.95	8.54	R0	⋯	*RHESSI*
2	3.15	5.28	R1	1.61	*RHESSI*
3	4.55	3.66	R2	2.33	*RHESSI*
4	5.78	2.88	R3	2.96	*RHESSI*
5	7.61	2.19	R4	3.89	*RHESSI*

P_1 is described by

$$P_1 = \frac{2L}{c_{\rm ph}}, \tag{8}$$

where $c_{\rm ph}$ is the phase speed, depending on the physical properties of the waveguide. The ratio of the period of the fundamental mode P_1 to the period of harmonics P_N is

$$\frac{P_1}{P_N} = N, \tag{9}$$

where $N > 1$ is an integer for uniform strings, representing the higher harmonic number. For a non-uniform string the period ratio may deviate from its canonical integer value given by Equation (9) above.

In our study, we propose that the observed oscillation pattern in flare occurrence is driven by the global oscillation of the solar atmosphere, manifested in periodic rearrangements of the magnetic field. Let us now model the *global*, large-scale solar atmosphere as a simple, uniform and homogeneous one-dimensional physical environment analog to the string example above. Here, the basic assumption is that this solar environment (shaken by a yet to be determined mechanism) responds as a global body to perturbations. Since the solar atmospheric plasma is embedded in a magnetic field, field lines will be shaken too, resulting in casual periodic reconnections that are observed as, e.g., *RHESSI* flares. Here, as a first approximation for insight, we ignore the complexity of active regions, stratification, and structuring. All these features influence the

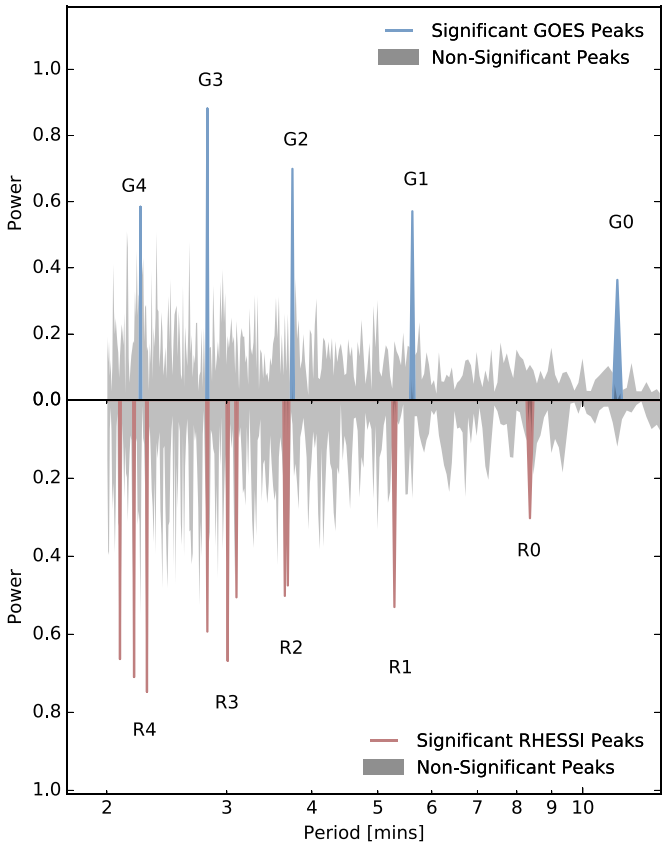

Figure 4. The top panel demonstrates the power spectrum of the *GOES* statistical sample. The bottom panel also visualizes the results of the FFT based on the *RHESSI* data. The silver peaks are marked as non-significant peaks and the blue and red peaks are greater than the 3σ significance threshold.

period ratio and eigenfunctions of the eigenmodes (in a flux tube and solar magnetoseismology context; see, e.g., Erdélyi & Verth 2007; Verth & Erdélyi 2008; Andries et al. 2009; Luna-Cardozo et al. 2012). Therefore, these omissions may need to be noted, and could be potentially important for a deeper diagnostic insight.

Here, we propose that the 3D magnetic solar atmosphere, in an active region, simply responds to some external driver (or drivers) as a resonator. The situation is very similar to that of the solar interior, addressed in great detail by the science of helioseismology. However, here magnetism is essential. In a sense, our modeling extends and generalizes the concept of

helioseismology by considering magnetism and applying it to the *upper* solar atmosphere as well. If our proposed thought experiment captures valid physics, and so far the indications of the detected frequencies are mounting evidence toward that, the interpretations of the solar flare observations have the potential to open up a very new branch of diagnostics in solar physics. The key reason this may be a major step for solar atmospheric diagnostics is that the deviation from the canonical values of frequency ratio can be directly linked to obtaining even sub-resolution information about the waveguide (Erdélyi & Verth 2007) associated P_1/P_N ratio of periods. In the *GOES* sample, the ratio of the fundamental mode period P_1 and the period of the first harmonic P_2 are around the canonical value of 2.01, indicating that there may not be large-scale strong inhomogeneity.

In general, with the current resolution we cannot yet determine with high confidence how much true deviation there is from this canonical value (referring to a uniform and homogeneous plasma). While the observed periods line up, as Table 3 shows, the P_1/P_N ratios follow an order of succeeding integer numbers only if we consider the *GOES* statistical sample. If the *GOES* fundamental period is taken into account as a *RHESSI* fundamental mode, the canonical values line up similarly as in the *GOES* sample. If the first significant *RHESSI* period *R*0 is considered the fundamental mode, the $P_1/P_2 = 1.61$ ratio significantly departs from a canonical value of 2, which may indicate inhomogeneity in the system.

5. Discussion

We need more insight into the nature of the underlying oscillations. Are they the result of Alfvén, slow, or fast standing MHD waves. Is there perhaps coupling between modes? What is the true geometry of the waveguide? More precisely, what is the waveguide? Is it bounded by the low photosphere and the upper turning point being the chromosphere, or are there other boundaries (reflective or open)? Are the modes linear or nonlinear? If the latter, this is a very difficult mathematical problem to model and proceed with. Answering all these questions suggests the direction of our future aims, because they may contribute to understanding the nature of the long-period global oscillations.

Improving our methodology is one of our future aims. Performing a wavelet analysis of the processed X-ray time-series may reveal information about period modulation. The detected oscillations may be present continuously around the major flare source and migrate to different frequencies over time. As Reznikova & Shibasaki (2011) concluded, the p-mode leakage upward along the active region magnetic field lines can play a role in the generation of periodic phenomena, particularly those with similar periods to those established in the present work. This needs to be further compared , since the presence of a global driver is more challenging to initiate, while sunspot p-mode waves are ubiquitous. Therefore, developing our physical interpretation and investigating other theories are also future aims.

It is also important to emphasize that the *GOES* and the *RHESSI* satellites observe at different wavelengths. It may be possible that discrepancies between the *GOES* oscillations and the *RHESSI* oscillations are the consequence of the different observational wavelengths, therefore the different wavelengths may reveal different physical processes.

6. Conclusion

We propose that X-ray flux oscillations are a consequence of global upper atmospheric oscillations and that, as said before, periodic reconnection is likely triggered by driving global atmospheric oscillations.

R.E. is grateful to STFC (UK), grant number ST/M000826/1, and The Royal Society for support received. This research has made use of SunPy, an open-source and free community-developed solar data analysis package written in Python (SunPy Community et al. 2015). The authors are indebted to the anonymous reviewer for providing insightful comments and directions for this paper.

References

Andries, J., van Doorsselaere, T., Roberts, B., et al. 2009, SSRv, 149, 3
Aschwanden, M. J., De Pontieu, B., Schrijver, C. J., et al. 2002, SoPh, 206, 99
Auchère, F., Bocchialini, K., Solomon, J., & Tison, E. 2014, A&A, 563, A8
Banerjee, D., Erdelyi, R., Oliver, R., & O'Shea, E. 2007, SoPh, 246, 3
Banerjee, D., Gupta, G., & Teriaca, L. 2011, SSRv, 158, 267
Bocchialini, K., Baudin, F., Koutchmy, S., Pouget, G., & Solomon, J. 2011, A&A, 533, A96
Charikov, Y. E. 2000, PCEC, 25, 407
Christe, S., Hannah, I., Krucker, S., McTiernan, J., & Lin, R. P. 2008, ApJ, 677, 1385
De Moortel, I. 2009, SSRv, 149, 65
DeForest, C., & Gurman, J. 1998, ApJL, 501, L217
Dolla, L., Marqué, C., Seaton, D. B., et al. 2012, ApJL, 749, L16
Erdélyi, R., & Taroyan, Y. 2008, A&A, 489, L49
Erdélyi, R., & Verth, G. 2007, A&A, 462, 743
Hurford, G. c., Schmahl, E., Schwartz, R., et al. 2003, The Reuven Ramaty High-Energy Solar Spectroscopic Imager (RHESSI) (Berlin: Springer), 61
Jess, D. B., Morton, R. J., Verth, G., et al. 2015, SSRv, 190, 103
Kasdin, N. J. 1995, Proc. IEEE, 83, 802
Lin, R., Dennis, B., Hurford, G., et al. 2002, SoPh, 210, 3
Luna-Cardozo, M., Verth, G., & Erdélyi, R. 2012, ApJ, 748, 110
Mathioudakis, M., Jess, D., & Erdelyi, R. 2013, SSRv, 175, 1
McLaughlin, J. A., Nakariakov, V. M., Dominique, M., Jelínek, P., & Takasao, S. 2018, SSRv, 214, 45
Mendoza-Briceño, C. A., Erdélyi, R., & Sigalotti, L. D. G. 2002, ApJL, 579, L49
Reznikova, V. E., & Shibasaki, K. 2011, A&A, 525, A112
Roberts, B., Edwin, P., & Benz, A. 1984, ApJ, 279, 857
Ruderman, M. S., & Erdélyi, R. 2009, SSRv, 149, 199
Simões, P. J. A., Hudson, H. S., & Fletcher, L. 2015, SoPh, 290, 3625
SunPy Community T., Mumford, S. J., Christe, S., et al. 2015, CS&D, 8, 014009
Sych, R., Karlický, M., Altyntsev, A., Dudík, J., & Kashapova, L. 2015, A&A, 577, A43
Sych, R., Nakariakov, V. M., Karlicky, M., & Anfinogentov, S. 2009, A&A, 505, 791
Tappin, S. 1991, A&AS, 87, 277
Taroyan, Y., Erdélyi, R., Doyle, J., & Bradshaw, S. 2005, A&A, 438, 713
Tian, H., Xia, L.-D., & Li, S. 2008, A&A, 489, 741
Verth, G., & Erdélyi, R. 2008, A&A, 486, 1015
Verth, G., Erdélyi, R., & Goossens, M. 2010, ApJ, 714, 1637
Wang, T. 2011, SSRv, 158, 397
Weedon, G. P. 2003, Time-series Analysis and Cyclostratigraphy: Examining Stratigraphic Records of Environmental Cycles (Cambridge: Cambridge Univ. Press)